AUT Journal of Electrical Engineering

AUT J. Elec. Eng., 49(1)(2017)75-84
DOI: 10.22060/eej.2016.11846.5008

A Miniaturized CPW-Fed Tapered Slot Antenna in Lossy Environment for UWB Application in Breast Cancer Detection

A. Hokmabadi[1*], A. Keshtkar[1], A. Bayat[1], A. Keshtkar[2]

[1] Electrical Engineering Department, Engineering Faculty, Imam Khomeini International University, Qazvin, Iran
[2] Medical Physics Department, Medical School, Tabriz University of Medical Sciences, Tabriz, Iran

ABSTRACT: In this paper, a miniaturized coplanar waveguide fed (CPW-fed) tapered slot antenna (TSA) is introduced for breast cancer detection. Here, a modified CPW to slot-line transition structure with an air-bridge is employed to broaden the transition bandwidth and increase the radiation efficiency. Through these applied modifications, negative features of the original TSA (limitation of transition) and antipodal Vivaldi antenna (bad cross-polarization) are both removed, while all the positive features remained. We have developed a FDTD-UPML method in lossy environment by using Debye model. To validate the results, a prototype of the proposed antenna is fabricated and tested. By immersing the antenna in alcohol ethanol as a lossy coupling medium and inserting it close to a two-layer breast phantom, near-field parameters are calculated in different probe locations. Results show that the proposed structure offers a broad bandwidth of 0.5–19 GHz and also exhibits an appropriate current distribution with high radiation efficiency. Images of energy flux density (EFD) and fidelity factor (FF) confirm the good performance of the antenna in near-field region.

Review History:
Received: 8 August 2016
Revised: 11 September 2016
Accepted: 27 February 2017
Available Online: 2 March 2017

Keywords:
breast cancer detection
CPW-fed
microwave imaging
tapered slot antenna (TSA)
Vivaldi

1- Introduction

Breast cancer is the most common type of cancer in women. Like many cancers, early detection is a fundamental factor in the long-time survival and quality of patient's life. Recently, microwave imaging for medical applications has received considerable attention [1-4]. The capability of penetrating waves into the breast, non-ionizing radiation, and possibility of high resolution through Ultra-wideband (UWB) technology, make this method an attractive alternative in breast cancer detection [5].

Microwave imaging relies on differences in the electrical properties of normal and malignant tissue through making maps of electrical property distribution in the body. The antenna design is one of the biggest challenges in microwave breast cancer detection. The antenna requires wide bandwidth, high efficiency in the frequency domain as well as good characteristic in the time-domain with minimal distortion. Moreover, the antenna should be immersed into a coupling medium with the permittivity similar to breast tissue to minimize the reflection between free space and tissue. Given that the antenna is placed very close to the breast, practically far-field parameters are not functional. Therefore, all the radiation requirements need to be fulfilled in the near field region. Size limitations as well as manufacturing cost are the other challenges in the design of antenna for medical applications.

Given the importance of the issue, many studies have been performed in this field [6-13]. In [6], by using stacked patches and thick substrate, the impedance bandwidth of antenna was increased. However, stacked patches create a potential of unwanted radiation at higher frequency. The proposed antennas in [7-9] provided a broad bandwidth. However, their low-end frequencies were not suitable to ensure sufficient penetration into the breast tissue. This problem was solved in [10, 11] by developing a compact bowtie antenna and analyzing an array of them near a phantom with embedded tumors. Despite worthwhile features, their directivity and gain were very low for lossy environment. The antipodal Vivaldi antenna (AVA) presented in [12] had high impedance bandwidth (2.1-27 GHz) as well as very good radiation characteristics. However, its cross to co-polarization component was very high that causes distortion in the time domain. In [13], a balanced antipodal Vivaldi antenna with a component named "director" (BAVA-D) was presented in which the near-field directivity was increased. Although the performance of this antenna was very good, but suffered from factors such as complex structure, large size and thickness that may increase the axial ratio followed by excitation of higher order modes [14].

Considering the results of the mentioned studies and other related publications, it can be concluded that basically Vivaldi antennas are one of the best candidates for imaging applications. This antenna was first introduced by Gibson [15], by which it was also known as the Vivaldi antenna, and many improvements to the initial design have been proposed since its introduction [16-21]. In [16, 17], two types of tapered slot antenna (TSA) including dual exponential TSA (DETSA) and dual V-type linear TSA (DVLTSA) were investigated. A simple design of a TSA using CPW for wide-slot transition was presented in [18]. This antenna exhibited a compact size and good gain, but its impedance bandwidth

Corresponding author; Email: hokmabadi@ikiu.ac.ir

and radiation efficiency were low. A miniaturized TSA, using a folded balun on the radiator, was proposed by Zhu et al. [19]. In [20, 21], a new method for the design of the flare's opening rate for a TSA was presented, and its UWB performance was evaluated. This method was based on a stepped quarter-wave Chebyshev transformer.

TSA can theoretically have unlimited bandwidth. But in practice, the microstrip to slot-line transition structure limits the high-end operating band. In addition, the width of the tapered flares limits the low-end operating band. The limitation of transition was later overcome in the AVA introduced in [22]. In recent years, several efforts have been made to optimize these antennas [23-28]. By using a high permittivity substrate and modification of the microstrip-fed structure, the physical size of the antenna was reduced [23]. In [24, 25], antenna size reduction and improvement of low-end radiation characteristics were performed using a tapered slot edge (TSE) technique. Generally, TSE structures improve the performance of low frequencies. Pandey et al. [26] proposed a novel compact AVA in the frequency range of 2–12 GHz. However, its realized gain and efficiency were low. Recently, a CPW-fed AVA with good radiation performance in the lower band was presented [27]. In [28] a modified compact AVA was proposed with a frequency band between 3.4–40 GHz. Despite AVA's worthwhile features, the inherent problem with AVA remains bad cross-polarization, especially for higher frequencies, due to the skew of the slot fields. By adding another layer to the AVA, a balanced antipodal Vivaldi antenna (BAVA) was created [13, 29], which offered low cross-polarization, but increased the complexity and cost, while also suffering from tilted beams.

One of the challenges of TSA design lies in its feeding structure. As mentioned, except for the limitation of transition, TSA performance is similar to AVA. Moreover, TSA cross-polarization remains very low. Therefore, the primary goal of this paper was to overcome the limitations in high and low-end bandwidth and increase the efficiency of the original TSA antenna, to maintain the good features of both TSA and AVA antennas. In this study, we have presented a modified CPW to slot-line transition. In the proposed design, the bandwidth of the transition is greatly enhanced by connecting one of the CPW arms to a broad-band open radial stub. Moreover, by adding an air-bridge the performance of the antenna is increased effectively in the lower frequencies. The antenna was immersed in the ethanol alcohol as the lossy coupling medium in order to get a good matching with the tissues of breast. Here, we have developed a finite-difference time-domain uniaxial perfectly matched layer (FDTD-UPML) code in lossy environment using first order Debye model. Moreover, experimental measurements and also CST simulations were performed to confirm the results. Energy flux density (EFD) and fidelity factor (FF) images of the antenna near a multilayer phantom of breast tissue were also calculated and compared with BAVA-D antenna proposed in [13]. In the following in section 2, the evaluation methods and FDTD-UPML formulation are presented. The antenna structure is presented in section 3. The results and discussion are described in section 4, and conclusions follow in section 5.

2- Evaluation Methods

In the proposed antenna, we have used Rogers RT/duroid 6010LM dielectric as a substrate with relative permittivity of 10.2. Since ε_r of this substrate is close to the real part of relative permittivity of the breast tissue [30], we have made such choice. Moreover, if a classical air matched antenna to be used for in-body medical applications, almost all the radiated field will be reflected at the air-skin interface, due to high difference in their dielectric parameters. Therefore, to avoid strong reflections and also increase dynamic range, a coupling medium between antenna and body is used. Coupling medium should be safe, cheap, and practical while providing acceptable matching with no loss. However, practically it is impossible to have a coupling medium without any loss. So, the permittivity of the coupling medium is given by

$\varepsilon_r^* = \varepsilon_r' - j\varepsilon_r''$, where ε_r' and ε_r'' are the real and imaginary part of the dielectric constant, respectively. The conductivity σ of the coupling medium is given by $\sigma = \omega\varepsilon_0\varepsilon_r''$. This conductivity causes the propagation constant appears as a complex value represented by

$$k_r' = \omega\sqrt{\mu_0\varepsilon_0(\varepsilon_r' - j\varepsilon_r'')} \quad (1)$$

Propagation constant changes will affect all the parameters of antenna such as input impedance, current distribution, and radiation pattern. In addition, we have to consider an additional loss due to the existence of coupling medium. According to [30], we have used ethanol alcohol (commercial grade) as the coupling medium. The complex permittivities of ethanol and body tissues are shown in Fig. 1. Moreover, first order Debye model is used to present property variations with frequency (Eq. (2)). In Table 1 ethanol, skin, and fat Debye parameters are listed. In order to simulate the performance of antenna, we have developed FDTD-UPML codes in lossy environment which are presented in the following.

$$\varepsilon_r^* = \varepsilon_\infty - j\frac{\sigma_s}{\omega\varepsilon_0} + \frac{\chi_1}{1+j\omega\tau} \text{ where } \chi_1 = \varepsilon_s - \varepsilon_\infty \quad (2)$$

In FDTD-UPML formulation, the Maxwell's curl equations in the lossy Debye medium can be expressed as follows [31]

$$\nabla\times\vec{H} = j\omega\varepsilon_0\varepsilon_r^*\overline{s}\vec{E}$$
$$\nabla\times\vec{E} = -j\omega\mu_0\overline{s}\vec{H} \quad (3)$$

Table 1. First order Debye model parameters of the materials.

Material	ε_∞	ε_s	τ (ps)	σ_s (S/m)
Breast (Fat)	7	10	7	0.15e-3
Skin	4	37	7.23	1.1
Ethanol	3.9	23.7	65	1e-3

where $\vec{E}$ and $\vec{H}$ are the electric and magnetic field intensity vectors and $\overline{s}$ is the diagonal tensor given by Eq. (4). This tensor is used to model the absorbing boundary conditions (ABC).

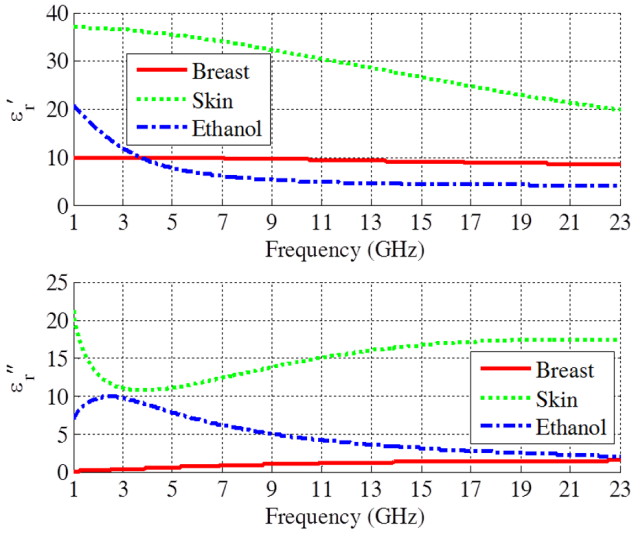

Fig. 1. Dielectric properties of the ethanol and body tissues.

$$\bar{s} = \begin{bmatrix} \frac{s_y s_z}{s_x} & 0 & 0 \\ 0 & \frac{s_x s_z}{s_y} & 0 \\ 0 & 0 & \frac{s_x s_y}{s_z} \end{bmatrix} \quad (4)$$

In Eq. (4) s_x, s_y, and s_z are the relative complex permittivities which are given by Eq. (5).

$$s_x = k_x + \frac{\sigma_x}{j\omega\varepsilon_0}$$
$$s_y = k_y + \frac{\sigma_y}{j\omega\varepsilon_0} \quad (5)$$
$$s_z = k_z + \frac{\sigma_z}{j\omega\varepsilon_0}$$

where k and σ at the outside of UPML band are zero. Through introducing intermediate variable F (Eq. (6)), the first formula of Eq. (3) can be expanded into three scalar partial differential equations (PDEs) as given in Eq. (7)

$$F_x = \frac{s_y s_z}{s_x} E_x \quad \& \quad F_y = \frac{s_x s_z}{s_y} E_y \quad \& \quad F_z = \frac{s_x s_y}{s_z} E_z \quad (6)$$

$$\begin{bmatrix} \frac{\partial H_z}{\partial y} - \frac{\partial H_y}{\partial z} \\ \frac{\partial H_x}{\partial z} - \frac{\partial H_z}{\partial x} \\ \frac{\partial H_y}{\partial x} - \frac{\partial H_x}{\partial y} \end{bmatrix} = j\omega\varepsilon_0\varepsilon_r^* \begin{bmatrix} F_x \\ F_y \\ F_z \end{bmatrix} \quad (7)$$

By substituting the Debye model (Eq. (2)) into Eq. (7), it can be converted into the time domain using the transformation $j\omega \to \frac{\partial}{\partial t}$. Finally, after discretization in the standard Yee-cell, the time stepping expressions for E_x, E_y, and E_z can be obtained. For example, the Ex updating equations are given below.

$$F_x^{n+1} = c_1 F_x^n + c_2 \left(\frac{\partial H_z}{\partial y} - \frac{\partial H_y}{\partial z} \right) + c_3 D_x^n$$

$$c_1 = \frac{2\tau\varepsilon_0\varepsilon_\infty - \sigma_s\tau\Delta t - \chi_1\varepsilon_0\Delta t}{2\tau\varepsilon_0\varepsilon_\infty + \sigma_s\tau\Delta t + \chi_1\varepsilon_0\Delta t}$$
$$c_2 = \frac{2\tau\Delta t}{2\tau\varepsilon_0\varepsilon_\infty + \sigma_s\tau\Delta t + \chi_1\varepsilon_0\Delta t} \quad (8)$$
$$c_3 = \frac{2\Delta t\chi_1\varepsilon_0}{2\tau\varepsilon_0\varepsilon_\infty + \sigma_s\tau\Delta t + \chi_1\varepsilon_0\Delta t}$$

$$D_x^{n+1} = \frac{2\tau - \Delta t}{2\tau + \Delta t} D_x^n + \frac{2\tau}{2\tau + \Delta t} F_x^{n+1} \quad (9)$$

$$G_x^{n+1} = \frac{2\varepsilon_0 k_y - \sigma_y\Delta t}{2\varepsilon_0 k_y + \sigma_y\Delta t} G_x^n + \frac{2\varepsilon_0}{2\varepsilon_0 k_y + \sigma_y\Delta t}\left(D_x^{n+1} - D_x^n\right) \quad (10)$$

$$E_x^{n+1} = \frac{2\varepsilon_0 k_z - \sigma_z\Delta t}{2\varepsilon_0 k_z + \sigma_z\Delta t} E_x^n + \frac{2\varepsilon_0 k_x + \sigma_x\Delta t}{2\varepsilon_0 k_z + \sigma_z\Delta t} G_x^{n+1} - \frac{2\varepsilon_0 k_x - \sigma_x\Delta t}{2\varepsilon_0 k_z + \sigma_z\Delta t} G_x^n \quad (11)$$

$$\Delta t = 1 \Big/ c\sqrt{1/\Delta x^2 + 1/\Delta y^2 + 1/\Delta z^2} \quad (12)$$

where Δx , Δy , and Δz are the dimensions of the Yee-cell and c is the velocity of light. The E_y and E_z components can be derived directly by substituting $x \to y \to z$ as right-hand rule. Also, update equations for H_x, H_y, and H_z components can be derived similar to derivation of Ex.

In order to compare the results, the simulations were done by CST Microwave Studio software, too. CST software has one and second order Debye models. The second order model is presented by Eq. (13)

$$\varepsilon_r^* = \varepsilon_\infty + \frac{\varepsilon_{s1} - \varepsilon_\infty}{1 + j\omega\tau_1} + \frac{\varepsilon_{s2} - \varepsilon_\infty}{1 + j\omega\tau_2} \quad (13)$$

Unfortunately, Eq. (13) does not include the ionic conductivity term (σ_s). To solve this problem, we have generated a table of materials property (ε^*_r) with a wide frequency range using the first order Debye model with ionic conductivity term according to Eq. (2). Then we have fitted a second order relaxation equation (Eq. (13)) to this data. The results are presented in Table 2.

Table 2. CST second order relaxation equation parameters.

Material	ε_∞	ε_{s1}	ε_{s2}	τ_1 (ps)	τ_2 (ps)
Breast (Fat)	7	8.5	8.5	7	7
Skin	4	51126.7	37	4.12e5	7.23
Ethanol	3.9	13.32	14.28	65	65

3- Antenna Structure

Configuration of the proposed TSA is shown in Fig. 2. The dimensions of the antenna were set to be 50 mm × 70 mm (0.08 λ × 0.12 λ; where λ is the wavelength of the low-end operating frequency). The proposed antenna is composed of three parts: feed line, radiating tapered slot, and CPW to slot-line transition structure which are described as follow

• Feed line: CPW line was used as feed line with a width of 0.4 mm, and a slot-line gap width of 0.8 mm, which its characteristic impedance matches with a 50 Ω, coaxial line. Moreover, as shown in Fig. 2, CPW center line and slot-line gap width decreases linearly to 0.1 mm and 0.2 mm, respectively. Through this method, we actually have made an impedance transformer for impedance matching between the CPW and the slot-line (42 Ω).

• Radiating tapered slot: The exponential curvatures in Fig. 2 indicate the radiating elements. These curvatures can be described by Eq. (14) which is widely used in many literatures [13, 24, 25].

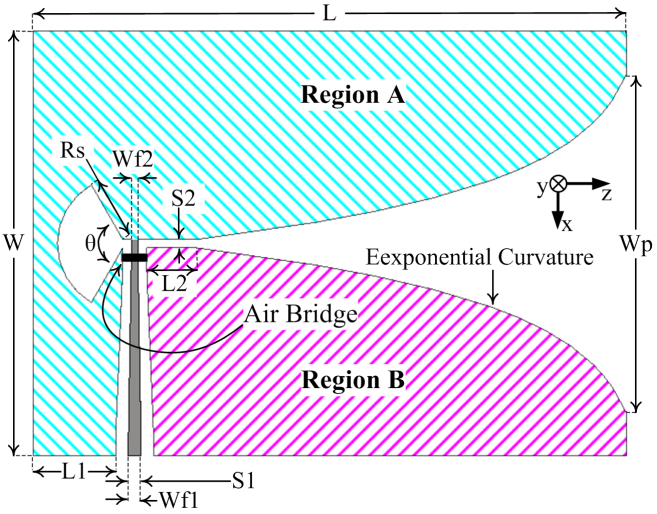

Fig. 2. Geometry of the proposed antenna.

$$x = Ae^{Rz} + B$$
$$A = \left(x_2 - x_1\right) \Big/ \left(e^{Rz_2} - e^{Rz_1}\right) \quad (13)$$
$$B = \left(x_1 e^{Rz_2} - x_2 e^{Rz_1}\right) \Big/ \left(e^{Rz_2} - e^{Rz_1}\right)$$

The points (x_1,z_1) and $(x_2,z2)$ are the end point of the flare and R is the opening rate of the exponential taper.

• CPW to slot-line transition: In the conventional microstrip to slot-line transition, two radial stubs, or circles, at opposite sides of the substrate were used for modelling the slot-line termination as an open circuit and the microstrip-line as a short circuit. However, in this paper, similar to [32, 33], we used only one radial stub at the end of the CPW single arm that acts as a broad-band open circuit. In previous works, this radial stub, or circle hollow, located asymmetrically with respect to the tapered flares, led to instability and deviation of the radiation pattern at different frequencies, and also limited the impedance bandwidth. Generally, due to the asymmetry in the feeding structure, symmetric radiation pattern is usually difficult to produce [34]. To solve this problem in our proposed antenna, the radial stub was located symmetrically, which caused the radiation pattern to be almost symmetrical with low deviation across the frequency band. Results showed that as the radius of the radial stub became larger, the return loss performance at the low and middle frequencies was better, but the high-end operating frequency decreased. Consequently, there was a trade-off.

In the proposed CPW antenna, a cross-section of tapered flares on each side of the slot (shaded A and B areas in Fig. 2) were not symmetrical or exactly the same. Because the electrical length of the two tapered flares was different, the waves propagated through them at different distances. This difference caused CPW-slot-line mode-conversion, and the experience of an unwanted current distribution and disturbance of current around the radial stub [region A in Fig. 3(a)]. To overcome this problem, we applied an air-bridge in the vicinity of the radial stub to connect the two tapered flares together (Fig. 2). The air-bridge exhibited a short circuit for the slot-line mode [35], and it united the two parts. This technique omitted the disturbance of current by directing the current toward the tapered flares, as shown in region B in Fig. 3(b).

The radiation efficiency in two situations, either with or without an air-bridge, is illustrated in Fig. 4. The plot shows that without an air-bridge the radiation efficiency is lower than 90% across a wide range of frequencies. On the other hand, adding the air-bridge increased the efficiency to more than 96% across almost the entire working frequency band. Instead of using an air-bridge, we also could connect two tapered flares at the other side of the substrate using via-holes. However, this technique increased both the complexity and cost of construction, while at higher frequencies the propagation characteristics of the via-holes have a stronger electromagnetic effect on the performance of the antenna that leads to gain reduction. Therefore, the air-bridge technique was a better choice.

Important advantages of the proposed transition are its simple design, low fabrication costs, uni-planar structure, low-wave propagation dispersion up to very high frequencies, and independence of via-holes. Moreover, CPW is not very sensitive to substrate thickness and allows a wide range of impedance values (20Ω -250Ω) on relatively thick substrates [36]. Therefore, it is preferable to microwave monolithic integrated circuit (MMIC) technologies.

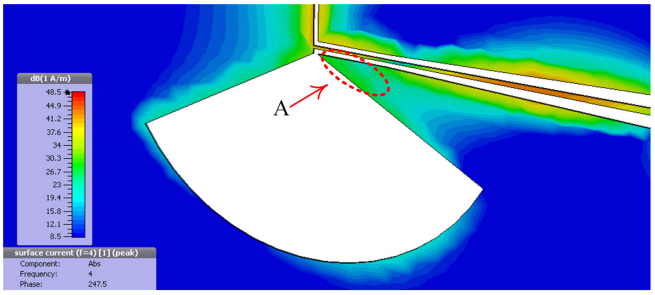

(a)

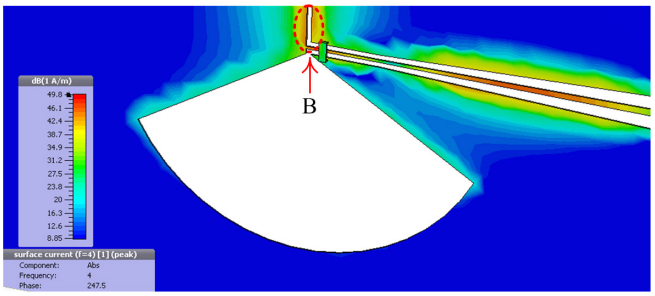

(b)

Fig. 3. Simulated current distribution of the antenna: (a) Without air-bridge; (b) With air-bridge.

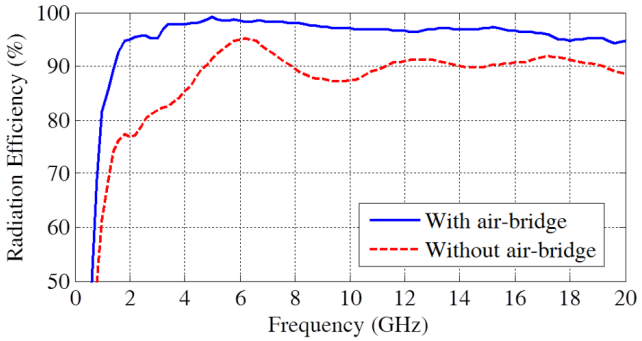

Fig. 4. Radiation efficiency of the antenna with and without an air-bridge.

4- Results And Discussion

After optimization by genetic algorithm with the cost function of maximum gain and minimum return loss, the final dimension values are listed in Table 3. To validate the results, a prototype of the proposed antenna is fabricated as shown in Fig. 5. A SMA connector is used to feed the antenna.

The simulated (FDTD-UPML) return loss in two situations, either with or without an air-bridge, are shown in Fig. 6. Moreover, to validate the results, the measured and CST simulated return losses are plotted in the same figure. As shown, the low-end operating band decreased from 2.1 GHz to 0.5 GHz, due to the presence of the air-bridge. However, the high-end operating band was also reduced a little, though that is not significant (from 19.6 GHz to 19 GHz). Extra simulation results showed that the width and height of the air-bridge does not have much influence on the overall performance of the antenna. However, the air-bridge worked better when it was not very close to the surface. FDTD-UPML and CST results almost provided the same high and low-end operating band with a similar behavior. However, a little incompatibility existed maybe due to the type and size of the mesh, position of the excitation signal, and difference in the type of methods (CST software is integral based, while FDTD-UPML is derivative based). In comparison between the measured and simulations results, we can see that the low-end operating band was the same. However, the high-end operating band in the measured results was higher than simulations (about 0.6 GHz). In the other frequencies, the measured result was in good agreement with the simulated results, but there were some deviations, perhaps due to multiple reflections caused by the SMA (SubMiniature version A) connector, the soldering process, or fabrication errors.

By employing a TSE structure, the electrical length of antenna can be increased, which in turn reduces the low-end frequency. In the proposed antenna, this frequency was low enough. Moreover, simulation results did not show a considerable effect. Therefore, in this study we did not apply the TSE structure.

Table 3. Optimal dimension values.

Dimension	Value (mm)	Dimension	Value (mm)
L	70	Wf1	0.4
L1	10.8	Wf2	0.1
L2	6	Wp	40
Rp	-0.15	S1	0.8
Rs	8	S2	0.2
W	50	θ	2π/3 (rad)

Based on IEEE Std C95.1, the maximum transmitted power into the body cannot be more than $P_t = -20\,\mathrm{dBW/cm^2}$ [37]. Accordingly, the antenna should be placed very close to the body. Therefore, all the radiation parameters of antenna need to be fulfilled in the near-field region. In the following, the near-field performance of the antenna is evaluated in terms of EFD and FF.

EFD is calculated by summing time samples of the instantaneous Poynting vector over duration of the simulation time (T_{sim}) (Eq. (15)) [13]

$$\mathrm{EFD}(x,y,z) = \int_0^{T_{sim}} \bar{E}(x,y,z,t) \times \bar{H}(x,y,z,t)\,dt \quad \left[\frac{J}{m^2}\right] \qquad (15)$$

The antenna was placed at a distance of 5 mm to a multilayer *skin+breast* phantom (Fig. 7). The skin and breast had 2 and 100 mm thickness, respectively. A set of probes in 10×10 matrix form were inserted at a distance of 50 mm from the skin layer inside the breast tissue in *xy* plane. So they were located 57 mm from the antenna in *z* direction. Moreover, two sets of *E* and *H* field probes were inserted in E-plane (*xoz*) and H-plane (*yoz*). The position of E and H field probes are plotted in Fig. 8.

Practically, due to lack of computer memory and processing power, it is not possible to use FDTD-UPML method for solving this large scale scenario. Moreover, Laboratory facilities to measure near-field parameters were not available. So, we have presented only the result of simulations done by CST. However, for the comparison, we have also calculated the results of BAVA-D antenna proposed in [13] for the same scenarios.

The normalized EFD results are shown in Fig. 9 in 2D space presentation. As expected, due to the existence of director, BAVA-D had more near-field directivity than our antenna in E- and H-plane. But in the *xy* plane @ z=57 mm, it can be seen that the total EFD of our antenna was more than BAVA-D and more power flowed toward the breast. For a better comparison, we mapped the 2D presentations in Fig. 9 to 1D presentations as depicted in Fig. 10. This was performed by calculating the mean of EFD as a function of radial distance from the origin of *xy* plane @ z = 57 mm cut-plane (Fig. 10(a)). Fig. 10(b)-(c) show the mean of EFD versus the distance from antenna aperture center. As seen in the figure, in all cases, the mean EFD of the proposed antenna was located at a higher energy level than BAVA-D antenna which implies the superiority of the proposed antenna. Moreover BAVA-D antenna had a 3-layer complicated structure while our antenna was a uni-planar simple design with low cost.

To calculate signal distortion in the time domain, a well-defined parameter named fidelity factor is proposed as given in Eq. (16) [38]

$$\mathrm{FF} = \max_{\tau}\left[\frac{\int_{-\infty}^{+\infty} s(t)r(t-\tau)\,dt}{\sqrt{\int_{-\infty}^{+\infty}\|s(t)\|^2\,dt}\sqrt{\int_{-\infty}^{+\infty}\|r(t)\|^2\,dt}}\right] \qquad (16)$$

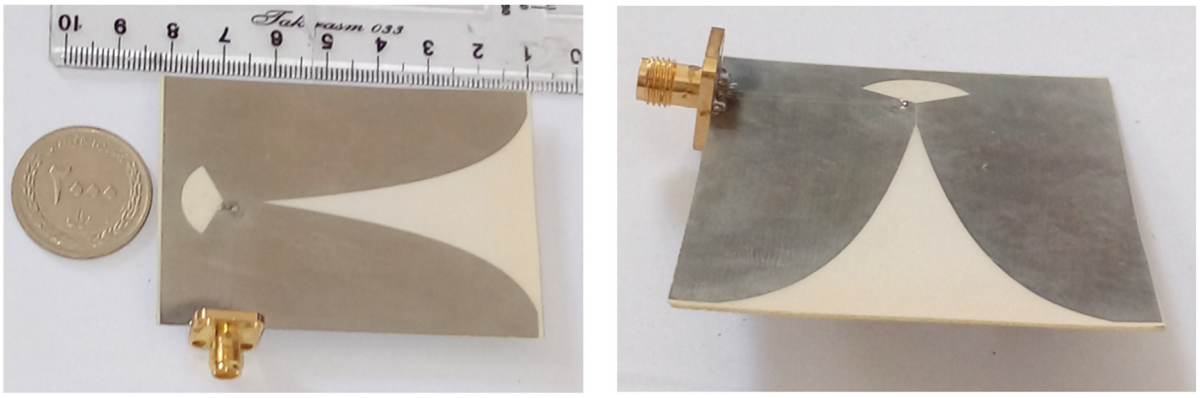

(a) (b)

Fig. 5. Fabricated prototype of the antenna: (a) Front view; (b) Top view.

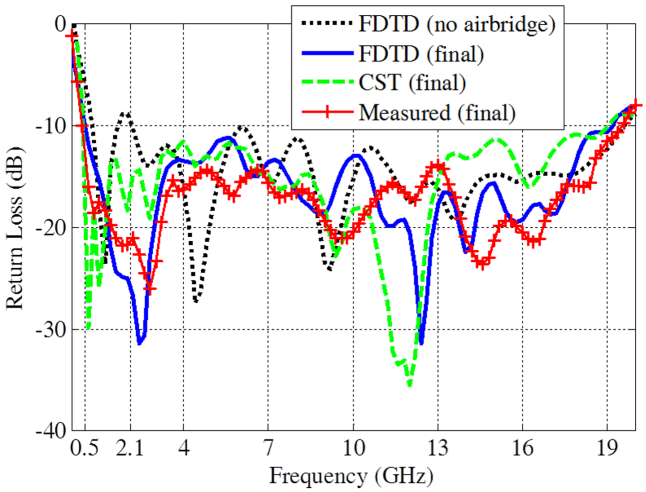

Fig. 6. Measured and simulated return loss.

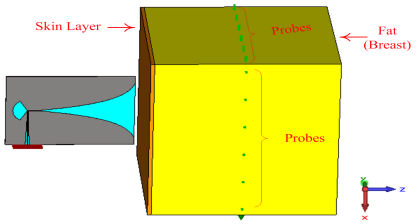

Fig. 7. Geometry of the antenna and skin+breast phantom.

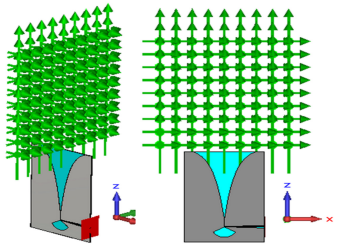

Fig. 8. Probes position in E- and H-plane.

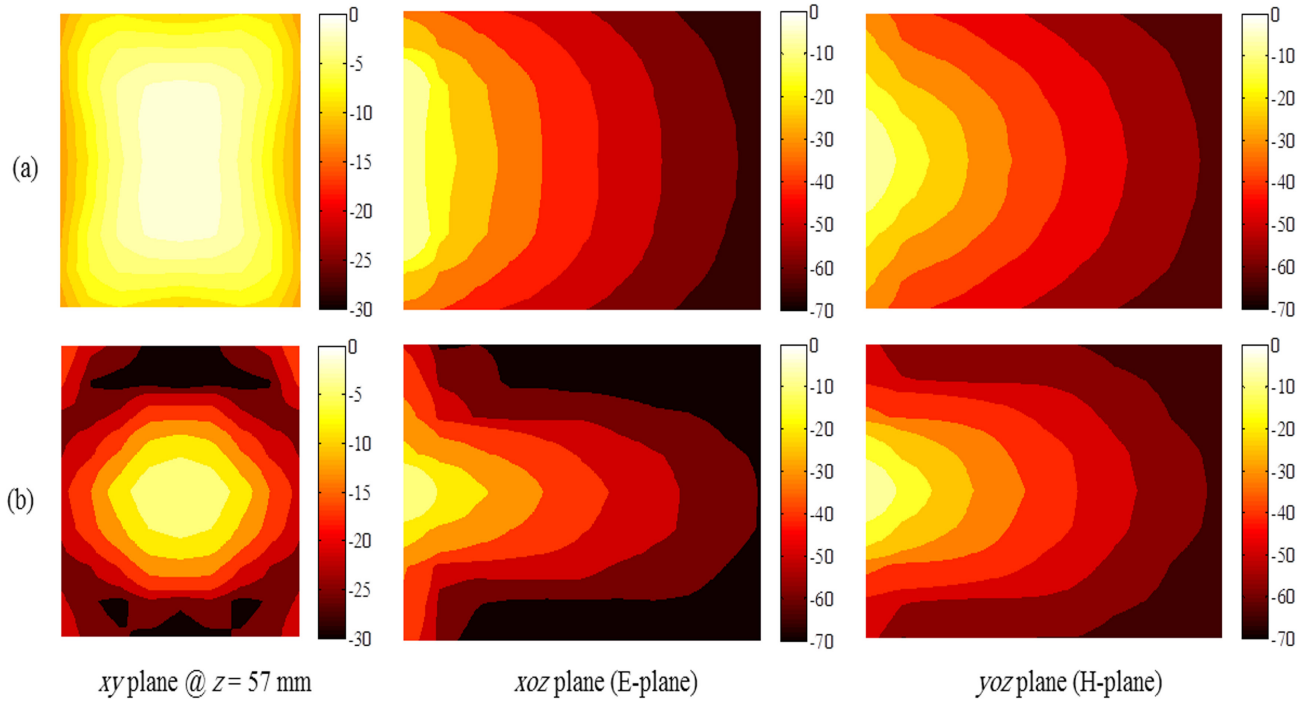

Fig. 9. EFD images in different planes: (a) Proposed antenna; (b) BAVA-D antenna.

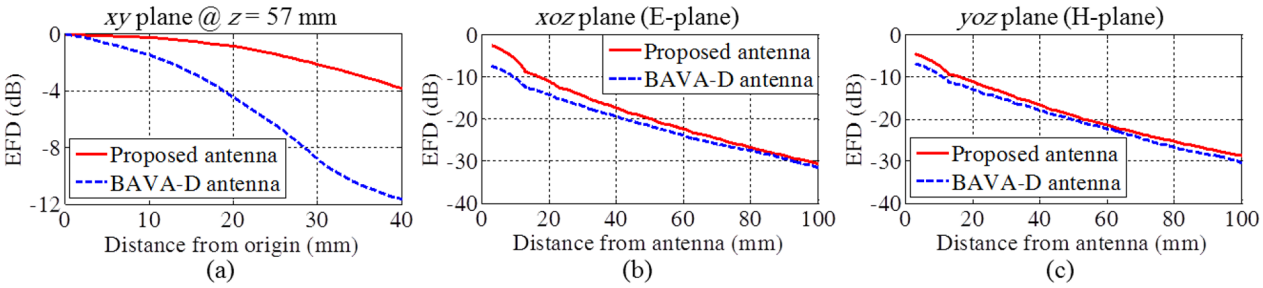

Fig. 10. Mean of EFD as a function of distance: (a) xy plane @ z = 57 mm; (b) E-plane; (c) H-plane.

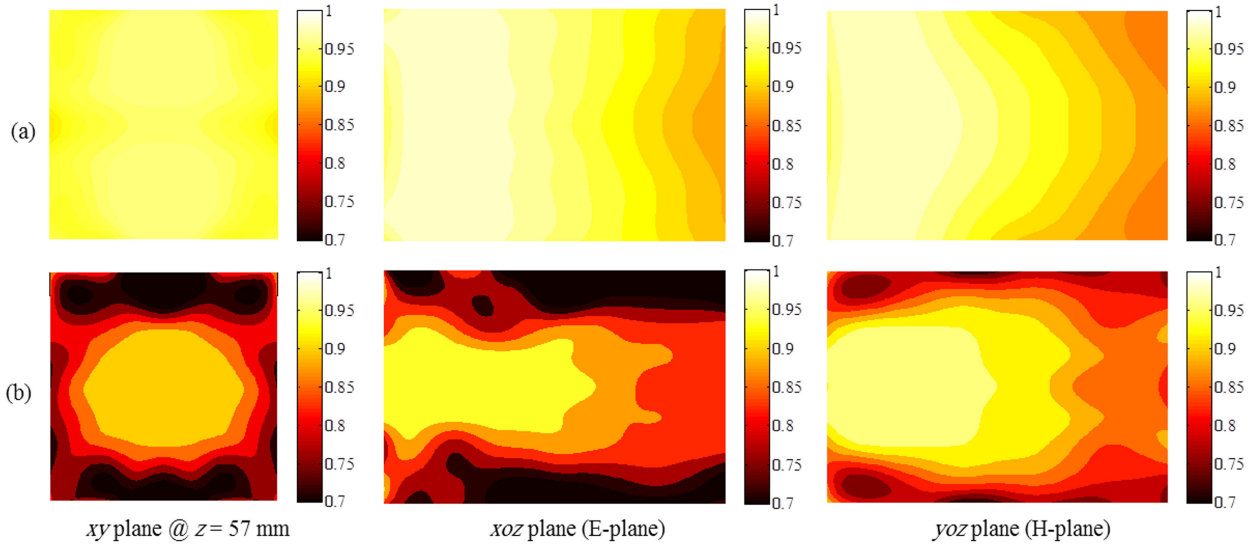

Fig. 11. FF images in different planes: (a) Proposed antenna; (b) BAVA-D antenna.

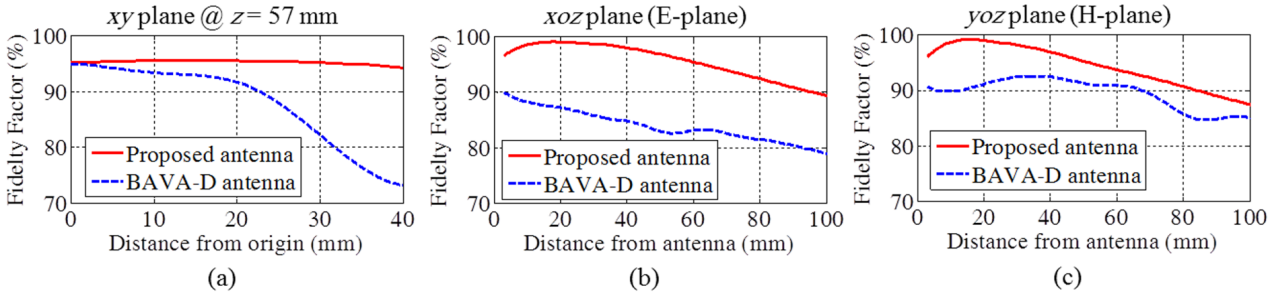

Fig. 12. Mean of FF as a function of distance: (a) xy plane @ z = 57 mm; (b) E-plane; (c) H-plane.

where s(t) is the excitation signal and r(t) is the received signal. The fidelity factor reflects the similarity between the source pulse and the radiated one. Here, in order to calculate the fidelity in different radiation directions, we have used the time domain waveform of the transmitted fields, recovered by the probes. The results are shown in Fig. 11. We can clearly see that the proposed antenna had a much better performance. In many locations of the probes the FF values were more than 0.95, while in BAVA-D antenna only around the z direction and just close to the antenna aperture, the FF values were about 0.9. It is while other locations of the probes suffered from high distortion. Here, as before the mapping from 2D to 1D space are performed in Fig. 12. As shown in this figure, the FF values of proposed antenna were very good and much better than ones in BAVA-D.

5- Conclusions

In this study, we proposed a miniaturized CPW-fed TSA. In this new proposed design, rather than using a conventional microstrip to slot-line transition, a modified CPW to slot-line transition with an air-bridge was employed. The proposed antenna has a compact size of 50 mm × 70 mm. A FDTD-UPML code was developed in lossy environment by using Debye model. The results of simulations and measurements showed that the antenna offers broad bandwidth of 189% over the interval from 0.5-19 GHz. This low-end frequency ensures sufficient penetration into the breast tissue. Moreover, the broad impedance bandwidth indicates good resolution of the system. Near-field characteristics of the antenna were analyzed while it was immersed in the lossy coupling medium (alcohol ethanol) and a two-layer breast phantom was located at the distance of 5 mm away. We have extracted EFD and FF images and compared them with the results of BAVA-D antenna. The results confirm good performance of the proposed antenna in the near-field region. All these properties make this antenna suitable for microwave imaging systems, particularly for breast cancer detection.

References

[1] A. H. Golnabi, P. M. Meaney, and K. D. Paulsen, "Tomographic Microwave Imaging With Incorporated Prior Spatial Information," IEEE Transactions on Microwave Theory and Techniques, vol. 61, pp. 2129-2136, 2013.

[2] E. Porter, E. Kirshin, A. Santorelli, M. Coates, and M. Popovi, "Time-Domain Multistatic Radar System for Microwave Breast Screening," IEEE Antennas and Wireless Propagation Letters, vol. 12, pp. 229-232, 2013.

[3] M. O. Halloran, E. Jones, and M. Glavin, "Quasi-Multistatic MIST Beamforming for the Early Detection of Breast Cancer," IEEE Transactions on Biomedical Engineering, vol. 57, pp. 830-840, 2010.

[4] A. Shahzad, M. O. Halloran, E. Jones, and M. Glavin, "Prefiltered Beamforming for Early-Stage Breast Cancer Detection," IEEE Antennas and Wireless Propagation Letters, vol. 12, pp. 500-503, 2013.

[5] A. M. Hassan and M. El-Shenawee, "Review of Electromagnetic Techniques for Breast Cancer Detection," IEEE Reviews in Biomedical Engineering, vol. 4, pp. 103-118, 2011.

[6] D. Gibbins, M. Klemm, I. J. Craddock, J. A. Leendertz, A. Preece, and R. Benjamin, "A Comparison of a Wide-Slot and a Stacked Patch Antenna for the Purpose of Breast Cancer Detection," IEEE Transactions on Antennas and Propagation, vol. 58, pp. 665-674, 2010.

[7] M. Bassi, M. Caruso, M. S. Khan, A. Bevilacqua, A. D. Capobianco, and A. Neviani, "An Integrated Microwave Imaging Radar With Planar Antennas for Breast Cancer Detection," IEEE Transactions on Microwave Theory and Techniques, vol. 61, pp. 2108-2118, 2013.

[8] T. Sugitani, S. Kubota, A. Toya, X. Xiao, and T. Kikkawa, "A Compact 4* 4 Planar UWB Antenna Array for 3-D Breast Cancer Detection," IEEE Antennas and Wireless Propagation Letters, vol. 12, pp. 733-736, 2013.

[9] C. H. See, R. A. Abd-Alhameed, S. W. J. Chung, D. Zhou, H. Al-Ahmad, and P. S. Excell, "The Design of a Resistively Loaded Bowtie Antenna for Applications in Breast Cancer Detection Systems," IEEE Transactions on Antennas and Propagation, vol. 60, pp. 2526-2530, 2012.

[10] M. Jalilvand, X. Li, J. Kowalewski, and T. Zwick, "Broadband miniaturised bow-tie antenna for 3D microwave tomography," Electronics Letters, vol. 50, pp. 244-246, 2014.

[11] M. Jalilvand, X. Li, L. Zwirello, and T. Zwick, "Ultra wideband compact near-field imaging system for breast cancer detection," IET Microwaves, Antennas & Propagation, vol. 9, pp. 1009-1014, 2015.

[12] M. Moosazadeh and S. Kharkovsky, "Design of Ultra-Wideband Antipodal Vivaldi Antenna for Microwave Imaging Applications," in 2015 IEEE International Conference on Ubiquitous Wireless Broadband (ICUWB), 2015, pp. 1-4.

[13] J. Bourqui, M. Okoniewski, and E. C. Fear, "Balanced Antipodal Vivaldi Antenna With Dielectric Director for Near-Field Microwave Imaging," IEEE Transactions on Antennas and Propagation, vol. 58, pp. 2318-2326, 2010.

[14] R. Telikepalli, "Design of a wide band microstrip patch for use in a phased array antenna for mobile satellite communications," in Electrical and Computer Engineering, 1995. Canadian Conference on, 1995, pp. 1173-1175 vol.2.

[15] P. J. Gibson, "The Vivaldi Aerial," in Microwave Conference, 1979. 9th European, 1979, pp. 101-105.

[16] G. E. Ponchak, J. L. Jordan, and C. T. Chevalier, "Characteristics of Double Exponentially Tapered Slot Antenna (DETSA) Conformed in the Longitudinal Direction Around a Cylinder," IEEE Antennas and Wireless Propagation Letters, vol. 6, pp. 60-63, 2007.

[17] Y. J. Cheng, W. Hong, and K. Wu, "Design of a Monopulse Antenna Using a Dual V-Type Linearly Tapered Slot Antenna (DVLTSA)," IEEE Transactions on Antennas and Propagation, vol. 56, pp. 2903-2909, 2008.

[18] H. Kim and C. W. Jung, "Ultra-wideband endfire directional tapered slot antenna using CPW to wide-slot transition," Electronics Letters, vol. 46, pp. 1183-1185, 2010.

[19] F. Zhu, S. Gao, A. T. S. Ho, R. A. Abd-Alhameed, C. H. See, J. Li, et al., "Miniaturized Tapered Slot Antenna With Signal Rejection in 5-6 GHz Band Using a Balun," IEEE Antennas and Wireless Propagation Letters, vol. 11, pp. 507-510, 2012.

[20] K. Ebnabbasi, D. Busuioc, R. Birken, and M. Wang, "Taper Design of Vivaldi and Co-Planar Tapered Slot Antenna (TSA) by Chebyshev Transformer," IEEE Transactions on Antennas and Propagation, vol. 60, pp. 2252-2259, 2012.

[21] K. Ebnabbasi, S. Sczyslo, and M. Mohebbi, "UWB Performance of Coplanar Tapered Slot Antennas," IEEE Antennas and Wireless Propagation Letters, vol. 12, pp. 749-752, 2013.

[22] E. Gazit, "Improved design of the Vivaldi antenna," IEE Proceedings H - Microwaves, Antennas and Propagation, vol. 135, pp. 89-92, 1988.

[23] A. M. Abbosh, "Miniaturized Microstrip-Fed Tapered-Slot Antenna With Ultrawideband Performance," IEEE Antennas and Wireless Propagation Letters, vol. 8, pp. 690-692, 2009.

[24] P. Fei, Y. C. Jiao, W. Hu, and F. S. Zhang, "A Miniaturized Antipodal Vivaldi Antenna With Improved Radiation Characteristics," IEEE Antennas and Wireless Propagation Letters, vol. 10, pp. 127-130, 2011.

[25] J. Bai, S. Shi, and D. W. Prather, "Modified Compact Antipodal Vivaldi Antenna for 4-50 GHz UWB Application," IEEE Transactions on Microwave Theory and Techniques, vol. 59, pp. 1051-1057, 2011.

[26] G. K. Pandey, H. Verma, and M. K. Meshram, "Compact antipodal Vivaldi antenna for UWB applications," Electronics Letters, vol. 51, pp. 308-310, 2015.

[27] Z. Wang, Y. Yin, J. Wu, and R. Lian, "A Miniaturized CPW-Fed Antipodal Vivaldi Antenna With Enhanced Radiation Performance for Wideband Applications," IEEE Antennas and Wireless Propagation Letters, vol. 15, pp. 16-19, 2016.

[28] M. Moosazadeh and S. Kharkovsky, "A Compact High-Gain and Front-to-Back Ratio Elliptically Tapered Antipodal Vivaldi Antenna With Trapezoid-Shaped Dielectric Lens," IEEE Antennas and Wireless Propagation Letters, vol. 15, pp. 552-555, 2016.

[29] J. D. S. Langley, P. S. Hall, and P. Newham, "Novel ultrawide-bandwidth Vivaldi antenna with low crosspolarisation,"

Electronics Letters, vol. 29, pp. 2004-2005, 1993.

[30] S. M. Salvador and G. Vecchi, "Experimental Tests of Microwave Breast Cancer Detection on Phantoms," IEEE Transactions on Antennas and Propagation, vol. 57, pp. 1705-1712, 2009.

[31] A. Taflove and S. Hagness, Computational Electrodynamics: The Finite-Difference Time-Domain Method, Third Edition: Artech House, 2005.

[32] K. Hettak, N. Dib, A. Sheta, A. A. Omar, G. Y. Delisle, M. Stubbs, et al., "New miniature broadband CPW-to-slotline transitions," IEEE Transactions on Microwave Theory and Techniques, vol. 48, pp. 138-146, 2000.

[33] T. Q. Ho and S. M. Hart, "A broad-band coplanar waveguide to slotline transition," IEEE Microwave and Guided Wave Letters, vol. 2, pp. 415-416, 1992.

[34] X. Ye, M. He, P. Zhou, and H. Sun, "A compact single-feed circularly polarized microstrip antenna with symmetric and wide-beamwidth radiation pattern," International Journal of Antennas and Propagation, vol. 2013, 2013.

[35] K. P. Ma, Y. Qian, and T. Itoh, "Analysis and applications of a new CPW-slotline transition," IEEE Transactions on Microwave Theory and Techniques, vol. 47, pp. 426-432, 1999.

[36] L. G. Maloratsky, Integrated Microwave Front-ends with Avionics Applications: Artech House, 2012.

[37] "Unapproved Revised Pc95.1b (Draft IEEE Standard for Safety Levels With Respect to Human Exposure to Radio Frequency Electromagnetic Fields, 3 kHz to 300 Ghz Amendment 1: Specific Absorption Rate (SAR) Limits for the Pinna) (Amendment 1 to IEEE Std C95.1-1991 (1999 Ed.) C95.1b) Replaced by Approved IEEE Draft," IEEE Std PC95.1/D2.4, p. 1, 2005.

[38] K. Do-Hoon, "Effect of antenna gain and group delay variations on pulse-preserving capabilities of ultrawideband antennas," IEEE Transactions on Antennas and Propagation, vol. 54, pp. 2208-2215, 2006.

Please cite this article using:

A. Hokmabadi, A. Keshtkar, A. Bayat, A. Keshtkar,"A Miniaturized CPW-Fed Tapered Slot Antenna in Lossy Environment for UWB Application in Breast Cancer Detection", *AUT J. Elec. Eng.*, 49(1)(2017)75-84.

DOI: 10.22060/eej.2016.11846.5008